

Bridging and depletion mechanisms in colloid-colloid effective interactions: A reentrant phase diagram

Riccardo Fantoni,^{1, a)} Achille Giacometti,^{2, b)} and Andrés Santos^{2, c)}

¹⁾ *Dipartimento di Scienze Molecolari e Nanosistemi, Università Ca' Foscari Venezia, Calle Larga S. Marta DD2137, I-30123 Venezia, Italy*

²⁾ *Departamento de Física and Instituto de Computación Científica Avanzada (ICCAEx), Universidad de Extremadura, E-06071 Badajoz, Spain*

(Dated: 11 July 2018)

A general class of nonadditive sticky-hard-sphere binary mixtures, where small and large spheres represent the solvent and the solute, respectively, is introduced. The solute-solute and solvent-solute interactions are of hard-sphere type, while the solute-solvent interactions are of sticky-hard-sphere type with tunable degrees of size nonadditivity and stickiness. Two particular and complementary limits are studied using analytical and semi-analytical tools. The first case is characterized by zero nonadditivity, lending itself to a Percus–Yevick approximate solution from which the impact of stickiness on the spinodal curves and on the effective solute-solute potential is analyzed. In the opposite nonadditive case, the solvent-solvent diameter is zero and the model can then be reckoned as an extension of the well-known Asakura–Oosawa model with additional sticky solute-solvent interaction. This latter model has the property that its exact effective one-component problem involves only solute-solute pair potentials for size ratios such that a solvent particle fits inside the interstitial region of three touching solutes. In particular, we explicitly identify the three competing physical mechanisms (depletion, pulling, and bridging) giving rise to the effective interaction. Some remarks on the phase diagram of these two complementary models are also addressed through the use of the Noro–Frenkel criterion and a first-order perturbation analysis. Our findings suggest reentrance of the fluid-fluid instability as solvent density (in the first model) or adhesion (in the second model) is varied. Some perspectives in terms of the interpretation of recent experimental studies of microgels adsorbed onto large polystyrene particles are discussed.

I. INTRODUCTION

Many years ago, Asakura and Oosawa¹ (AO) provided an explanation of the clustering and gelation phenomenon occurring when small nonadsorbing polymers, such as polystyrene (PS), were added to a solution of large spherical colloids, say polymethylmethacrylate (PMMA). The basic idea is illustrated in Fig. 1 considering two PMMA colloids, modeled as big spheres, immersed in a fluid formed by a uniform background (that we will neglect henceforth) as well as by PS particles, assumed to be small *noninteracting spheres* that, however, experience a hard-sphere (HS) interaction with the larger ones. Under these conditions, when the separation between the two large spheres is less than the diameter of the small spheres (see Fig. 1), there is an unbalanced pressure of the “sea” of small spheres, providing an entropic gain compared to the case when the separation is large, that can be reckoned as an *effective* attractive interaction driving the clustering of large colloidal spheres.

In real systems, however, the solvent particles do not always behave as an ideal gas or interact only sterically. Typically, they experience an additional short-range attraction (or repulsion) with the solute, usually due to dis-

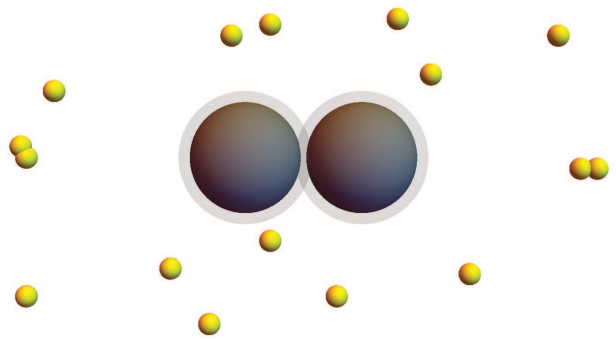


FIG. 1. Cartoon of the AO depletion interaction. The shaded region around each solute represents the volume excluded to the centers of the solvent particles.²

persion forces.^{3–6} The simplest way of accounting for a short-range solute-solvent attraction is by means of Baxter’s sticky-hard-sphere (SHS) model⁷ characterized by a stickiness parameter τ_{sl} . Both issues (solvent-solvent repulsion and solute-solvent short-range attraction) were recently addressed by two experimental studies^{8,9} on adsorbing microgels (MG) to large PS latex suspension. In this case, the expected mechanism will be clearly different, as illustrated by Fig. 2, inspired by a similar figure of Ref. 8.

Let σ_l and σ_s be the diameters of the large and small spheres, respectively, and suppose we fix the volume fraction η_l of the large colloidal spheres and gradually increase the volume fraction η_s of the small solvent spheres.

^{a)} Electronic mail: rfantoni@ts.infn.it

^{b)} Electronic mail: achille.giacometti@unive.it

^{c)} Electronic mail: andres@unex.es; <http://www.unex.es/eweb/fisteor/andres>

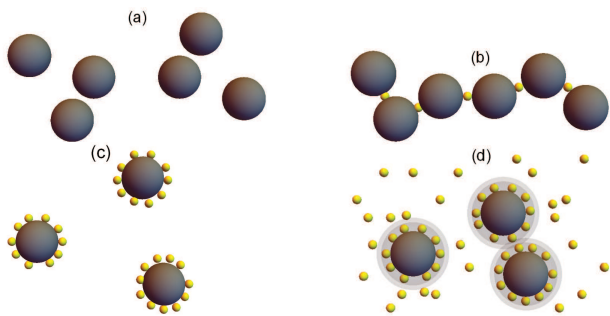


FIG. 2. Different mechanisms occurring in the presence of a short-range attraction between solvent and solute, as the solvent concentration increases: (a) $\eta_s = 0$, HS behavior; (b) $0 < \eta_s < \eta_s^*$, the small fraction of solvent particles act as bridges connecting the solute into a cluster; (c) $\eta_s \approx \eta_s^*$, most of the solute colloids are covered and again behave as HSs with an effective diameter $\sigma_s + \sigma_l$; (d) $\eta_s > \eta_s^*$, the “dressed” solutes feel an effective depletion attraction. The dark and light shaded regions around the solute particles in panel (d) represent the effective solute size and the effective volume excluded to the centers of the solvent particles, respectively.

In the absence of solvent particles, the solute particles will behave essentially as HSs, as depicted in Fig. 2(a). Now imagine we gradually add the small solvent particles. Because of the solute-solvent attraction, they will tend to get adsorbed on the surface of the larger particles and mediate an effective attraction between them. This *bridging* mechanism destabilizes the solution as the large colloidal spheres tend to form aggregates, as schematically illustrated in Fig. 2(b). The global effect is the formation of a *gel* phase caused by a free-energy driven phase separation of the large and small spheres. As η_s increases, solvent particles tend to progressively cover the solute surface, as depicted in Fig. 2(c). We can easily estimate¹⁰ the critical value η_s^* at which all large spheres will be completely covered to be $\eta_s^* \approx \eta_l(2\pi/\sqrt{3})\sigma_s/\sigma_l$, as discussed in Appendix A. At this point, all the solute colloids can be “fully covered” by solvent particles and they will behave essentially again as HSs with an effective diameter $\sigma_l + \sigma_s$, with a few additional free solvent particles. This situation is pictured in Fig. 2(c). Upon adding further solvent particles, however, depletion forces between the small and the covered colloids set in [Fig. 2(d)] and phase separation occurs again, this time entropically rather than free-energetically, as in the case of Fig. 2(b). A useful way to represent the phase diagram of such a binary mixture is through an (η_l, η_s) diagram at fixed values of size ratio $q = \sigma_s/\sigma_l$ and stickiness τ_{sl}^{-1} . In this diagram, there will be geometrically inaccessible regions, for example for η_s or η_l larger than $\pi/3\sqrt{2}$, and lines separating the various phase coexistence regions. The topology of the phase diagram would be controlled by q , while η_s would play the role of an inverse temperature.

Motivated by these new experimental perspectives, recently Chen et al.¹¹ considered a HS-SHS binary mixture where one can tune the attraction parameter τ_{sl} between

the unlike spheres, with like spheres only interacting via HS interactions. Note that this is the same model already studied by Fantoni et al.,¹² as well as by other groups.²⁹ The study of Ref. 11 provided a well defined framework to rationalize the experimental results obtained in Refs. 8 and 9.

In the present work, we will build upon this idea and go further to introduce also an additional—and, to the best of our knowledge, new—model that has the interesting feature of including the standard AO model^{1,11} as a particular case. In both cases, we will illustrate how an effective one-component solute-solute interaction potential can be obtained and the merits and drawbacks of this procedure.

Both models can be seen as extreme realizations of a general class of nonadditive sticky-hard-sphere (NASHS) binary mixtures where the small-small (or solvent-solvent) and large-large (or solute-solute) interactions are of HS type with diameters σ_{ss} and $\sigma_{ll} = \sigma_l$, respectively, while the small-large (or solvent-solute) interactions are of SHS type characterized by a cross diameter $\sigma_{sl} = (\sigma_s + \sigma_l)/2 = \sigma_l(1 + q)/2$ and an inverse stickiness τ_{sl} . Note that here we denote by $\sigma_s = q\sigma_l$ the diameter of the small spheres *as seen* by the large ones, while σ_{ss} is the diameter of the small spheres as seen by themselves. Thus, the nonadditivity of the unlike interactions is monitored by the ratio $\sigma_{ss}/\sigma_s \leq 1$ (where we have restricted ourselves to zero or positive nonadditivity). The NASHS class reduces to the nonadditive hard-sphere (NAHS) class if the solute-solvent stickiness is switched off.

In the first model that we will study one has $\sigma_{ss}/\sigma_s = 1$, so that the HS interactions are additive. This model, denoted henceforth as the additive sticky-hard-sphere (ASHS) model, is the one depicted in Fig. 2 and considered in Refs. 11 and 12. Interestingly, the ASHS model can be solved exactly within the Percus–Yevick (PY) approximation^{12–15} and the instability region in the (η_s, η_l) plane enclosed by the spinodal line can be computed. This will be found to form a closed region, in agreement with previous results.¹¹

The second model represents an extreme case of positive nonadditivity, namely $\sigma_{ss}/\sigma_s = 0$, i.e., the solvent spheres behave among themselves as an ideal gas. This particular case of the general class of NASHS models reduces to the conventional AO model if the stickiness is switched off (i.e., $\tau_{sl} \rightarrow \infty$). Because of that, we will term this model as the sticky Asakura–Oosawa (SAO) model. The need of supplementing the AO model with a short-range solute-solvent attraction has been recognized, for instance, in Ref. 5. While, in contrast to the ASHS model, the SAO model does not allow for an analytical solution in the PY approximation, its associated *effective* solute-solute pair potential can be exactly derived in the semi-grand-canonical ensemble, analogously to the case of the pure AO model.^{16–18} Moreover, and also in analogy with the AO model,^{17,19–21} such a pair potential turns out to be the only one contributing to

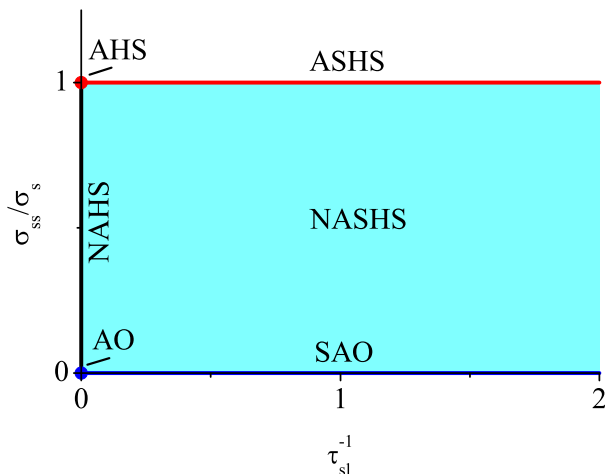


FIG. 3. Plane σ_{ss}/σ_s vs τ_{sl}^{-1} sketching different models mentioned in the text. The general class of NASHS models include, as limiting cases, ASHS ($\sigma_{ss}/\sigma_s = 1$), SAO ($\sigma_{ss}/\sigma_s = 0$), and NAHS ($\tau_{sl}^{-1} = 0$). The intersection of the NAHS line with the ASHS and SAO lines define the AHS and AO models, respectively. In this paper, we will be concerned with the ASHS and SAO models.

the exact effective interaction among the solutes if the size ratio $q = \sigma_s/\sigma_l$ is smaller than the threshold value $q_0 = 2/\sqrt{3} - 1 \approx 0.1547$. A careful comparison between the results of the two models (ASHS and SAO) allows us to pave the way for an improved theoretical understanding of the above experiments.

It is interesting to observe that, when the solute-solvent adhesion is set to zero, the model ASHS reduces to a size-asymmetric additive HS (AHS) binary mixture, while the SAO model becomes the original AO model, these two mixtures having quite different critical behaviors upon varying q .^{16,17,22} The metastable fluid-fluid demixing coexistence, responsible for the broadening at $\eta_s > 0$ of the stable fluid-solid coexistence ($0.492 \leq \eta_l \leq 0.543$) for pure HSs ($\eta_s \rightarrow 0$),^{23,24} remains always metastable and exists at small enough q in the AHS case, whereas it becomes stable at large q in the AO case, where a triple point appears. Figure 3 sketches (in the plane σ_{ss}/σ_s vs τ_{sl}^{-1}) the different models referred to above.

The organization of this paper is as follows. Section II presents the problem of the effective solute interaction mediated by the solvent particles within a general framework. This is followed by Sec. III, where the PY solution for the ASHS model is exploited to find the spinodal curves of the original mixture and the effective solute-solute pair potential. The exact derivation of the effective potential in the SAO model with a size ratio $q < q_0$ is addressed in Sec. IV, its three contributions being clearly identified. Next, the different scenarios for criticality in the ASHS and SAO effective systems are analyzed via the second virial coefficient and the Noro-Frenkel criterion²⁵ in Sec. V. A more detailed analysis for the SAO model

is performed via a first-order perturbation theory in Sec. VI. Finally, our findings are discussed and put in perspective in Sec. VII. The most technical details are relegated to four appendices.

II. GENERAL FRAMEWORK

Consider a colloidal binary mixture of N_s small (solvent) and N_l large (solute) particles, identified by the coordinates $\{\mathbf{r}_1^{(s)}, \mathbf{r}_2^{(s)}, \dots, \mathbf{r}_{N_s}^{(s)}\}$ and $\{\mathbf{r}_1^{(l)}, \mathbf{r}_2^{(l)}, \dots, \mathbf{r}_{N_l}^{(l)}\}$, respectively, in a volume V .

Assuming pair interactions, i.e., assuming the particles are nondeformable, nonpolarizable, \dots , (see Ref. 26 for a recent discussion on the reliability of this assumption), the total potential U can be written as $U = U_{ss} + U_{ll} + U_{sl}$, where

$$U_{ss} = \sum_{i=1}^{N_s-1} \sum_{j=i+1}^{N_s} \varphi_{ss}(|\mathbf{r}_i^{(s)} - \mathbf{r}_j^{(s)}|), \quad (2.1)$$

$$U_{ll} = \sum_{i=1}^{N_l-1} \sum_{j=i+1}^{N_l} \varphi_{ll}(|\mathbf{r}_i^{(l)} - \mathbf{r}_j^{(l)}|), \quad (2.2)$$

$$U_{sl} = \sum_{i=1}^{N_s} \sum_{j=1}^{N_l} \varphi_{sl}(|\mathbf{r}_i^{(s)} - \mathbf{r}_j^{(l)}|). \quad (2.3)$$

The canonical free energy $F(N_s, N_l, V, T)$ is then given by

$$e^{-\beta F} = \frac{\Lambda_s^{-3N_s} \Lambda_l^{-3N_l}}{N_s! N_l!} \int d\mathbf{r}^{N_s} \int d\mathbf{r}^{N_l} e^{-\beta(U_{ss} + U_{ll} + U_{sl})}, \quad (2.4)$$

where $\beta = 1/k_B T$ (k_B being the Boltzmann constant), Λ_s and Λ_l are the de Broglie thermal wavelengths associated with the small and large particles, respectively, and we have used the short-hand notation $d\mathbf{r}^{N_\alpha} = d\mathbf{r}_1^{(\alpha)} \dots d\mathbf{r}_{N_\alpha}^{(\alpha)}$ with $\alpha = s, l$.

Following standard prescriptions,^{16,17,27} one can in principle trace out all the microscopic degrees of freedom associated with the solvent particles and recast Eq. (2.4) in a form of an *effective* one-component system for only the solute particles with a potential energy $U_{ll}^{\text{eff}}(\mathbf{r}_1^{(l)}, \mathbf{r}_2^{(l)}, \dots, \mathbf{r}_{N_l}^{(l)})$. More specifically,

$$e^{-\beta U_{ll}^{\text{eff}}} = \frac{e^{-\beta U_{ll}}}{N_s! \Lambda_s^{3N_s}} \int d\mathbf{r}^{N_s} e^{-\beta(U_{ss} + U_{sl})}, \quad (2.5)$$

so that, Eq. (2.4) becomes

$$e^{-\beta F} = \frac{1}{N_l! \Lambda_l^{3N_l}} \int d\mathbf{r}^{N_l} e^{-\beta U_{ll}^{\text{eff}}}. \quad (2.6)$$

In general, however, the effective potential U_{ll}^{eff} is not pairwise additive, meaning that apart from pair-interaction terms (and less relevant zero- and one-body terms), it requires three-body, four-body, \dots terms.

Thus, the general structure of U_l^{eff} would be

$$U_l^{\text{eff}} = N_l v_l^{(0)} + \sum_{i=1}^{N_l} v_l^{(1)}(\mathbf{r}_i^{(l)}) + \sum_{i<j}^{N_l} v_l^{(2)}(|\mathbf{r}_i^{(l)} - \mathbf{r}_j^{(l)}|) + \sum_{i<j<k}^{N_l} v_l^{(3)}(\mathbf{r}_i^{(l)}, \mathbf{r}_j^{(l)}, \mathbf{r}_k^{(l)}) + \dots \quad (2.7)$$

The physically most relevant contribution is expected to be the one associated with the effective *pair* potential $v_{ll}(r) \equiv v_{ll}^{(2)}(r)$, in which case one can approximately neglect $v_{ll}^{(n)}$ with $n \geq 3$.

Now we specialize to the general class of NASHS models described in Sec. I. The $\varphi_{ss}(r)$ and $\varphi_{ll}(r)$ pair interactions are of HS type characterized by diameters σ_{ss} and σ_{ll} , respectively, while the small-large interaction $\varphi_{sl}(r)$ is of SHS type^{7,28} with a hard-core distance σ_{sl} and a stickiness parameter τ_{sl}^{-1} , the latter measuring the strength of surface adhesiveness. Therefore, the relevant Mayer functions $f_{\alpha\gamma}(r) = e^{-\beta\varphi_{\alpha\gamma}(r)} - 1$ are

$$f_{ss}(r) = -\Theta(\sigma_{ss} - r), \quad (2.8)$$

$$f_{ll}(r) = -\Theta(\sigma_{ll} - r), \quad (2.9)$$

$$f_{sl}(r) = -\Theta(\sigma_{sl} - r) + \frac{\sigma_{sl}}{12\tau_{sl}}\delta(r - \sigma_{sl}). \quad (2.10)$$

Here, $\Theta(x)$ is the Heaviside step function and $\delta(x)$ is the Dirac delta function. To simplify the notation, we adopt the viewpoint of the large spheres by calling $\sigma_l = \sigma_{ll}$ their diameter and defining σ_s as the diameter of the small spheres as felt by the large ones, so that $\sigma_{sl} = (\sigma_s + \sigma_l)/2$. Thus, the size asymmetry of the mixture (again from the viewpoint of the solute particles) is measured by the ratio $q = \sigma_s/\sigma_l < 1$, while the nonadditivity of the hard-core interactions is measured by the ratio $\sigma_{ss}/\sigma_s \leq 1$ (where, as said before, we discard here the case of negative non-additivity). For later use, let us introduce the partial packing fraction of species α as $\eta_\alpha = \pi\rho_\alpha\sigma_\alpha^3/6$, where $x_\alpha = N_\alpha/N$ is the concentration of species $\alpha = s, l$ and $\rho_\alpha = N_\alpha/V$ is its density. The total number of particles and number density of the fluid mixture are $N = N_l + N_s$ and $\rho = N/V$, respectively.

As discussed in Sec. I, we now particularize to two interesting particular cases that are identified by the ratio σ_{ss}/σ_s : the ASHS model (where $\sigma_{ss}/\sigma_s = 1$) and the SAO model (where $\sigma_{ss}/\sigma_s = 0$). The first model was studied before by two of us (it was called System A in Sec. V of Ref. 12) and has been rejuvenated by a recent study by Chen et al.¹¹ The second model is an extension of the well-known AO model, except that a sticky (or adhesive) interaction exists between the solvent and the solute particles. To the best of our knowledge, it has not been studied before. In both cases we will be able to derive the effective pair potential $v_{ll}(r) = v_{ll}^{(2)}(r)$ [see Eq. (2.7)] either within the PY approximation in the canonical ensemble (ASHS model) or in an exact way in the semi-grand-canonical ensemble (SAO model).

III. THE PY APPROXIMATE SOLUTION OF THE ASHS MODEL

The solution of the PY approximation for the ASHS model was recently studied in Ref. 12. The PY solution actually extends to the more general formulation where the Baxter stickiness coefficient^{7,28} between a particle of species α and one of species γ is $\tau_{\alpha\gamma}^{-1}$.¹³⁻¹⁵ Since here we choose $\tau_{ss} \rightarrow \infty$ and $\tau_{ll} \rightarrow \infty$, we can only have adhesion between unlike particles and $\tau_{sl}^{-1} > 0$ measures its strength.

A. Spinodal curve

From Eq. (85) of Ref. 12 we find the following expression for the spinodal of the full binary mixture in the (η_s, η_l) plane, as obtained from the PY approximation,

$$\tau_{sl}^{\text{sp}}(\eta_s, \eta_l) = \left[\frac{1 + (1+q)(1-\eta_s-\eta_l)/3(\eta_s+q\eta_l)}{1 + \sqrt{\left(1 + \frac{1-\eta_s-\eta_l}{3\eta_s}\right)\left(1 + \frac{1-\eta_s-\eta_l}{3\eta_l}\right)}} - 1 \right] \times \frac{(1+q)(\eta_s+q\eta_l)}{4q(1-\eta_s-\eta_l)}, \quad (3.1)$$

which, as it should, is symmetric under the exchange $\eta_s \leftrightarrow \eta_l$ and $q \leftrightarrow 1/q$. For a fixed q , there is a maximum value of τ_{sl}^{sp} for which Eq. (3.1) admits a solution with $\eta_s > 0$ and $\eta_l > 0$. We will denote this maximum value with $\tilde{\tau}_{sl}$ and the corresponding solution, the critical point, with $(\tilde{\eta}_s, \tilde{\eta}_l)$. In particular, at $q = q_0$ we find $\tilde{\tau}_{sl} = 0.014448$, $\tilde{\eta}_s = 0.019839$, and $\tilde{\eta}_l = 0.101645$. For $\tau_{sl} < \tilde{\tau}_{sl}$ the solution of Eq. (3.1) is a closed curve in the (η_s, η_l) plane within which the thermodynamically unstable region lies, as shown in Fig. 4. As we can see, the spinodal curve does not change much for $\tau_{sl} < 0.001$, where it is crossed by the straight line representing the critical packing fraction $\eta_s = \eta_s^*$. These findings are in complete agreement with those reported in Ref. 11.

Note that Eq. (3.1) is a particular case of an equation for a general mixture derived by Barbooy and Tenne,²⁹ that should however be handled with great care.³⁰

B. Approximate effective one-component fluid

As explained in Sec. II, one could in principle integrate out the solvent degrees of freedom to obtain the effective solute potential U_l^{eff} [see Eqs. (2.5) and (2.7)]. Here we want to focus on the *pair* interaction potential $v_{ll}(r) = v_{ll}^{(2)}(r)$. This function can be identified from the solute-solute radial distribution function $g_{ll}(r)$ in the infinite dilution limit ($x_l \rightarrow 0$) since in that limit only pair interactions contribute to $g_{ll}(r)$. Therefore, $g_{ll}(r) \rightarrow e^{-\beta v_{ll}(r)}$ and hence

$$\beta v_{ll}(r) = - \lim_{x_l \rightarrow 0} \ln g_{ll}(r). \quad (3.2)$$

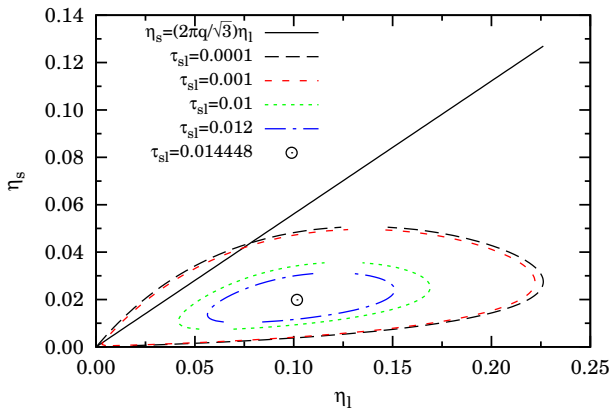


FIG. 4. PY spinodal for $q = q_0$ and several values of τ_{sl} . The straight line is $\eta_s = \eta_s^*$ and the circle is the critical point at $\tau_{sl} = 0.014448$.

In the limit of no adhesion ($\tau_{sl} \rightarrow \infty$), $v_{ll}(r)$ becomes the usual depletion potential.^{31,32} For further use, we will refer to *entropic* regime as the one with $\tau_{sl} \gg 1$, close to a size-asymmetric binary HS mixture. Reciprocally, the *nonentropic* regime will refer to a system with a small τ_{sl} . The *transitional* regime will correspond to $\tau_{sl} \sim 1$.

Since η_s is supposed to be finite in Eq. (3.2), it is not possible to obtain the exact effective pair potential $v_{ll}(r)$. On the other hand, it can be obtained again from the PY solution, as described in Appendix B. Note that, although the infinite dilution limit is applied as a shortcut to derive the pair potential $v_{ll}(r)$, at a nonzero solute concentration the full effective many-body potential U_{ll}^{eff} includes nonpairwise terms, as represented by $v_{ll}^{(3)}(\mathbf{r}_i, \mathbf{r}_j, \mathbf{r}_k)$ and higher-order terms in Eq. (2.7).

In Fig. 5 we report a few representative examples of the effective solute-solute pair potential corresponding to the ASHS model in the PY approximation (see Appendix B). Figure 5(a) shows the influence of the solute-solvent stickiness at fixed $\eta_s = 0.1$ and $q = q_0$. One can clearly observe the different shape of the potential in the entropic ($\tau_{sl} = 10^4$), transitional ($\tau_{sl} = 1$), and nonentropic ($\tau_{sl} = 0.12$) regimes. In the former case ($\tau_{sl} = 10^4$), the potential is essentially attractive (except for a slight hump in the region $r/\sigma_l \lesssim 1+q$), thus reflecting the depletion mechanisms (see Fig. 1). Moreover, at this very high value of τ_{sl} , the discontinuity of the potential at $r/\sigma_l = 1+q$ [see Eq. (B15)] is not visible. In the transitional regime ($\tau_{sl} = 1$), however, the discontinuity at $r/\sigma_l = 1+q$ is already noticeable and the potential in most of the inner region $1 < r/\sigma_l < 1+q$ has changed from attractive to repulsive. These two features are widely enhanced in the nonentropic regime ($\tau_{sl} = 0.12$): there is a high discontinuity at $r/\sigma_l = 1+q$ and the effective potential is strongly repulsive in the whole region $1 < r/\sigma_l < 1+q$. Furthermore, a strong repulsion appears as well in the outer region $r/\sigma_l \gtrsim 1+q$. Figure 5(b) shows that an increase of the solvent density magnifies the characteristic features of the effective po-

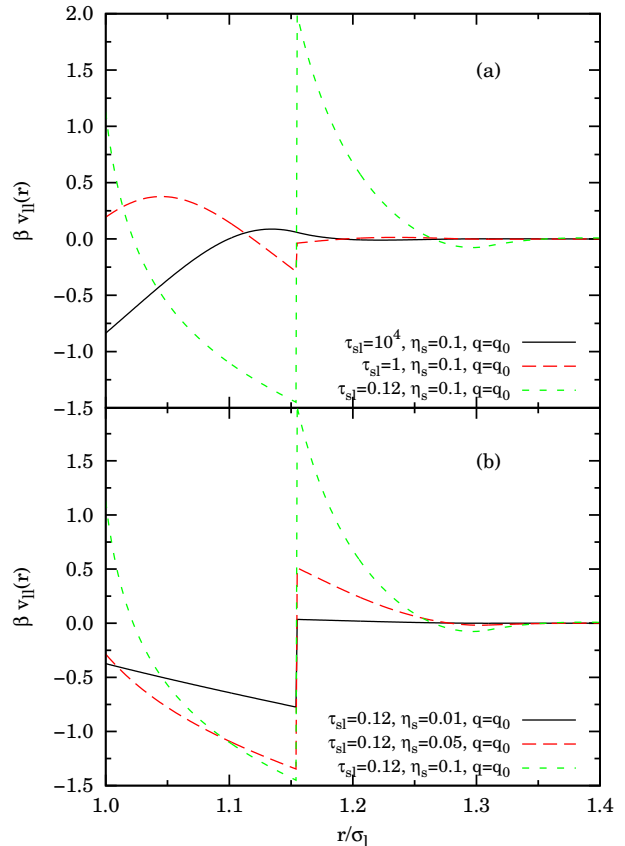


FIG. 5. Effective solute-solute pair potential in the ASHS model, as obtained from the PY approximation (see Appendix B). In panel (a) the stickiness parameter is varied at a fixed solvent packing fraction $\eta_s = 0.1$, while in panel (b), η_s is varied at fixed $\tau_{sl} = 0.12$. In all the cases the size ratio is $q = q_0$.

tential in the nonentropic regime. The physical origin of the repulsive regions in the nonentropic regime can be ascribed to the net *pulling* role played by the solvent particles attached to the two solutes. This effect will be identified more clearly in the SAO model (see Sec. IV). As for the (attractive) discontinuity at $r/\sigma_l = 1+q$, it can be attributed to the *bridging* effect of solvent particles attached to both solutes. This bridging mechanism is absent if $r/\sigma_l = (1+q)^+$ but appears if $r/\sigma_l = (1+q)^-$.

Dijkstra et al.^{16,27} already showed that the effective potential in the entropic regime is unable to produce a stable demixing phase transition with reasonably small q . On the other hand, the step attraction at $r/\sigma_l = 1+q$ in the potential associated with the nonentropic regime can lead to a demixing transition, as shown in Ref. 12. This is the phase instability studied in the (η_s, η_l) plane in Sec. III A.

With all due cares, the shape of the effective potential in the nonentropic regime depicted in Fig. 5(b) can be *schematically* represented as a square-well (SW) potential of width $q\sigma_l$ and depth $\epsilon \sim |v_{ll}(\sigma_l(1+q)^-)|$, with an additional repulsive tail starting at $r = \sigma_l(1+q)^+$.

We can then exploit the fact that the phase behavior of a one-component SW fluid is well established.^{33–36} For example, it is sufficient to heuristically consider the approximate critical value³⁵ of the reduced temperature $T^* = k_B T / \epsilon$ to find the appearance of an open phase coexistence region at high η_s (well separated from the closed one predicted in Sec. III A at low η_s). This coexistence region is known to be present in the highly asymmetric AHS mixture^{16,27} (i.e., for small q in the limit $\tau_{sl} \rightarrow \infty$). The effective problem procedure that we followed suggests that, quite intuitively, such a region will not disappear when the attraction is switched on at small τ_{sl} . It is interesting to observe that such a reentrance at large η_s is not predicted by an analysis of the behavior of the effective second virial coefficient B_2^{eff} [see Eq. (B16)], according to which $1/T^* = \ln [1 + (1 - B_2^{\text{eff}}/B_2^{\text{HS}})/(3q + 3q^2 + q^3)]$, where $B_2^{\text{HS}} = \frac{2\pi}{3}\sigma_l^3$. The two heuristic criteria based on an effective SW temperature T^* agree quite well for small values of η_s [as expected from the curve $\eta_s = 0.01$ in Fig. 5(b)], but the B_2^{eff} criterion presents a diverging T^* at a value of η_s such that $B_2^{\text{eff}} = B_2^{\text{HS}}$ and becomes meaningless thereafter (i.e., when $B_2^{\text{eff}} > B_2^{\text{HS}}$). For instance, if $q = q_0$ and $\tau_{sl} = 0.12$, the condition $B_2^{\text{eff}} > B_2^{\text{HS}}$ is satisfied for $\eta_s > 0.274$. The fact that $B_2^{\text{eff}} > B_2^{\text{HS}}$ if η_s is large enough is directly related to the increase of the effective size of the *dressed* solute particles, as depicted in Figs. 2(c) and 2(d).

Of course, the effective one-component fluid is not fully equivalent to the original binary mixture, as we are neglecting three-body (and higher) terms in the effective total potential [see Eq. (2.7)]. Moreover, the potentials of Fig. 5 are the outcome of the PY approximation. Yet, they are expected to give reasonable approximate results in the spirit of an effective fluid. Chen et al.¹¹ devised a similar approximate mapping of the PY solution for the true binary mixture onto a one-component SHS model, from which they were able to read-off the binodal using accurate Monte Carlo (MC) results by Miller and Frenkel.³⁷

While some caution must be exercised when using the pairwise potential formally obtained in the limit $\eta_l \rightarrow 0$ to predict the phase diagram at finite η_l , this keeps being a useful procedure to reduce the complexity of the binary mixture problem,³⁸ allowing one to get additional physical insight without the need, for example, of performing computer simulations of the full binary mixture.

IV. THE SAO MODEL

As shown in Sec. III, the ASHS model ($\sigma_{ss}/\sigma_s = 1$) admits a PY analytical solution but only an approximate reduction to an effective one-component fluid. The SAO model ($\sigma_{ss}/\sigma_s = 0$) is, in some sense, complementary to it, as it does not admit an analytical solution, not even in the PY approximation, but it does admit an exact reduction to an effective one-component fluid for

$q < q_0 = 2/\sqrt{3} - 1 \simeq 0.1547$, when a solvent particle can fit into the inner volume created by three solutes at contact,³⁹ so that a solvent particle cannot overlap simultaneously with more than two (nonoverlapping) solute particles. This corresponds to $q < 1$ in one spatial dimension.⁴⁰

To proceed, it is convenient to change from the canonical (N_s, N_l, V, T) ensemble to the semi-grand-canonical (μ_s, N_l, V, T) ensemble,^{16,17} where μ_s is the chemical potential of the solvent component. The corresponding thermodynamic potential $\mathcal{F}(\mu_s, N_l, V, T)$ is constructed via the Legendre transform

$$\mathcal{F}(\mu_s, N_l, V, T) = F(\langle N_s \rangle, N_l, V, T) - \mu_s \langle N_s \rangle. \quad (4.1)$$

Thus, the counterpart of canonical Eq. (2.4) is

$$\begin{aligned} e^{-\beta\mathcal{F}} &= \sum_{N_s=0}^{\infty} \frac{z_s^{N_s}}{N_s! N_l! \Lambda_l^{3N_l}} \int d\mathbf{r}^{N_s} \int d\mathbf{r}^{N_l} e^{-\beta(U_{ll} + U_{sl})} \\ &= \frac{1}{N_l! \Lambda_l^{3N_l}} \int d\mathbf{r}^{N_l} e^{-\beta U_{ll}^{\text{eff}}}, \end{aligned} \quad (4.2)$$

where

$$z_s = \frac{e^{\beta\mu_s}}{\Lambda_s^3} \quad (4.3)$$

is the solvent fugacity and

$$e^{-\beta U_{ll}^{\text{eff}}} = e^{-\beta U_{ll}} \sum_{N_s=0}^{\infty} \frac{z_s^{N_s}}{N_s!} \int d\mathbf{r}^{N_s} e^{-\beta U_{sl}}. \quad (4.4)$$

Note that in Eq. (4.2) we have taken into account that $U_{ss} = 0$ in the SAO model.

Inserting Eq. (2.3) into Eq. (4.4) it is easy to obtain¹⁷

$$\beta\Omega = -z_s \int d\mathbf{r} \prod_{i=1}^{N_l} \left[1 + f_{sl}(|\mathbf{r} - \mathbf{r}_i^{(l)}|) \right], \quad (4.5)$$

where $\Omega = U_{ll}^{\text{eff}} - U_{ll}$ represents the grand potential of an ideal gas of solvent particles in the external field of a fixed configuration of N_l solute particles with coordinates $\{\mathbf{r}_i^{(l)}\}$. Expanding in products of Mayer functions, Ω can be written as

$$\Omega = \sum_{n=0}^{n_{\text{max}}(q)} \Omega_n. \quad (4.6)$$

Here, Ω_n is the contribution to Ω stemming from the product of n Mayer functions f_{sl} . The upper limit $n_{\text{max}}(q)$ is the maximum number of nonoverlapping solutes that can simultaneously overlap with a single solvent particle. For $n > n_{\text{max}}(q)$, at least one of the factors f_{sl} vanishes and so does Ω_n . If $q < q_0$, then $n_{\text{max}}(q) = 2$, implying that the exact effective potential U_{ll}^{eff} does not include three-body (or higher order) terms. In the interval $q_0 < q \leq 1$, $n_{\text{max}}(q)$ grows by steps as q increases, reaching a maximum value $n_{\text{max}}(q) = 11$ (since a solvent

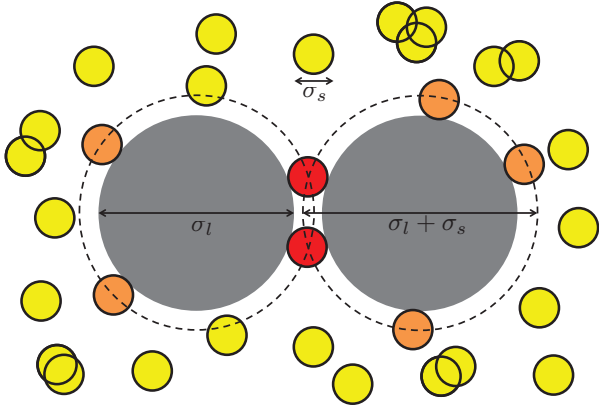


FIG. 6. Cartoon describing the three effects (depletion, pulling, and bridging) contributing to the effective solute-solute interaction in the SAO model. The grey large spheres represent the solutes of diameter σ_l at a distance $r < \sigma_l + \sigma_s = \sigma_l(1 + q)$. They are surrounded by a sea of smaller spheres (the solvent) of diameter $\sigma_s = q\sigma_l$ ($q = 0.2$ in the cartoon) that can overlap among themselves and have a sticky surface (represented by a thick perimeter). Some of the solvent particles (the yellow ones) do not touch the solutes and so they contribute to the (attractive) depletion effect, which is represented by $\psi_d(r)$, a volumetric term independent of τ_{sl} . Other solvent particles (the orange ones) are adhered to one of the big spheres, thus contributing to the (repulsive) pulling effect, represented by $\psi_p(r)$, which is a surface term proportional to τ_{sl}^{-1} . Finally, some other small particles (the red ones) are adhered to both solutes, giving rise to the (attractive) bridging effect, represented by $\psi_b(r)$, which is a line (intersection of two surfaces) term proportional to τ_{sl}^{-2} .

particle can simultaneously overlap with 12 nonoverlapping solutes only if $q > 1$). The first few terms in Eq. (4.6) are

$$\beta\Omega_0 = -z_s V, \quad (4.7)$$

$$\beta\Omega_1 = -z_s \sum_{i=1}^{N_i} \int d\mathbf{r} f_{sl}(|\mathbf{r} - \mathbf{r}_i^{(l)}|), \quad (4.8)$$

$$\begin{aligned} \beta\Omega_2 &= -z_s \sum_{i < j}^{N_i} \int d\mathbf{r} f_{sl}(|\mathbf{r} - \mathbf{r}_i^{(l)}|) f_{sl}(|\mathbf{r} - \mathbf{r}_j^{(l)}|) \\ &= \beta \sum_{i < j}^{N_i} \left[v_{ll}(|\mathbf{r}_i^{(l)} - \mathbf{r}_j^{(l)}|) - \varphi_{ll}(|\mathbf{r}_i^{(l)} - \mathbf{r}_j^{(l)}|) \right] \end{aligned} \quad (4.9)$$

Equation (4.9) allows us to identify the exact effective pair potential as

$$\beta v_{ll}(r) = \beta \varphi_{ll}(r) - z_s \int d\mathbf{r}_s f_{sl}(r_s) f_{sl}(|\mathbf{r}_s - \mathbf{r}|). \quad (4.10)$$

Now, making use of Eq. (2.10), one can obtain

$$\beta\Omega_1 = z_s \eta_l V (1 + q)^3 \left(1 - \frac{1}{4\tau_{sl}} \right), \quad (4.11)$$

$$\beta v_{ll}(r) = \eta_s^{(r)} \begin{cases} \infty, & r < \sigma_l, \\ \psi(r), & \sigma_l < r < \sigma_l(1 + q), \\ 0, & r > \sigma_l(1 + q), \end{cases} \quad (4.12)$$

where $\eta_s^{(r)} = z_s(\pi/6)\sigma_s^3$ is the (nominal) solvent packing fraction of a *reservoir* made of noninteracting solvent particles and

$$\psi(r) = \psi_d(r) + \psi_p(r) + \psi_b(r) \quad (4.13)$$

with

$$\begin{aligned} \psi_d(r) &= -\frac{6}{\pi\sigma_s^3} \int d\mathbf{r}_s \Theta(\sigma_{sl} - r_s) \Theta(\sigma_{sl} - |\mathbf{r}_s - \mathbf{r}|) \\ &= -\frac{(1 + q - r/\sigma_l)^2 (2 + 2q + r/\sigma_l)}{2q^3}, \end{aligned} \quad (4.14)$$

$$\begin{aligned} \psi_p(r) &= \frac{\sigma_{sl}}{\pi\sigma_s^3\tau_{sl}} \int d\mathbf{r}_s \delta(r_s - \sigma_{sl}) \Theta(\sigma_{sl} - |\mathbf{r}_s - \mathbf{r}|) \\ &= \frac{(1 + q)^2 (1 + q - r/\sigma_l)}{4q^3\tau_{sl}}, \end{aligned} \quad (4.15)$$

$$\begin{aligned} \psi_b(r) &= -\frac{\sigma_{sl}^2}{24\pi\sigma_s^3\tau_{sl}^2} \int d\mathbf{r}_s \delta(r_s - \sigma_{sl}) \delta(|\mathbf{r}_s - \mathbf{r}| - \sigma_{sl}) \\ &= -\frac{(1 + q)^4}{192q^3\tau_{sl}^2 r/\sigma_l}. \end{aligned} \quad (4.16)$$

The effective solute-solute force $f_{ll}(r) = -\partial v_{ll}(r)/\partial r$ (outside the hard core, $r > \sigma_l$) is

$$\begin{aligned} \frac{\beta f_{ll}(r)}{\eta_s^{(r)}} &= -[\psi_d'(r) + \psi_p'(r) + \psi_b'(r)] \Theta(1 + q - r/\sigma_l) \\ &\quad - \frac{(1 + q)^3}{192q^3\tau_{sl}^2} \delta(r - \sigma_l(1 + q)), \end{aligned} \quad (4.17)$$

where the delta term reflects the discontinuity of $v_{ll}(r)$ at $r = \sigma_l(1 + q)$ and

$$\psi_d'(r) = \frac{3}{2q^3\sigma_l} \left[(1 + q)^2 - \frac{r^2}{\sigma_l^2} \right], \quad (4.18)$$

$$\psi_p'(r) = -\frac{(1 + q)^2}{4q^3\sigma_l\tau_{sl}}, \quad \psi_b'(r) = \frac{(1 + q)^4}{192q^3\tau_{sl}^2 r^2/\sigma_l}, \quad (4.19)$$

If $q < q_0$, the general relationship between the reservoir packing fraction $\eta_s^{(r)}$ (or, equivalently, the fugacity z_s) and the values η_s and η_l of the binary mixture is derived in Appendix C with the result

$$\begin{aligned} \eta_s &= \eta_s^{(r)} \left[1 - \eta_l(1 + q)^3 \left(1 - \frac{1}{4\tau_{sl}} \right) - \frac{12\eta_l^2 q^3}{\sigma_l^3} \right. \\ &\quad \left. \times \int_{\sigma_l}^{\sigma_l(1+q)} dr r^2 \psi(r) g_{\text{eff}}(r|\eta_l, \eta_s^{(r)}) \right], \end{aligned} \quad (4.20)$$

where $g_{\text{eff}}(r|\eta_l, \eta_s^{(r)})$ is the radial distribution function of a pure fluid of large particles interacting via the effective

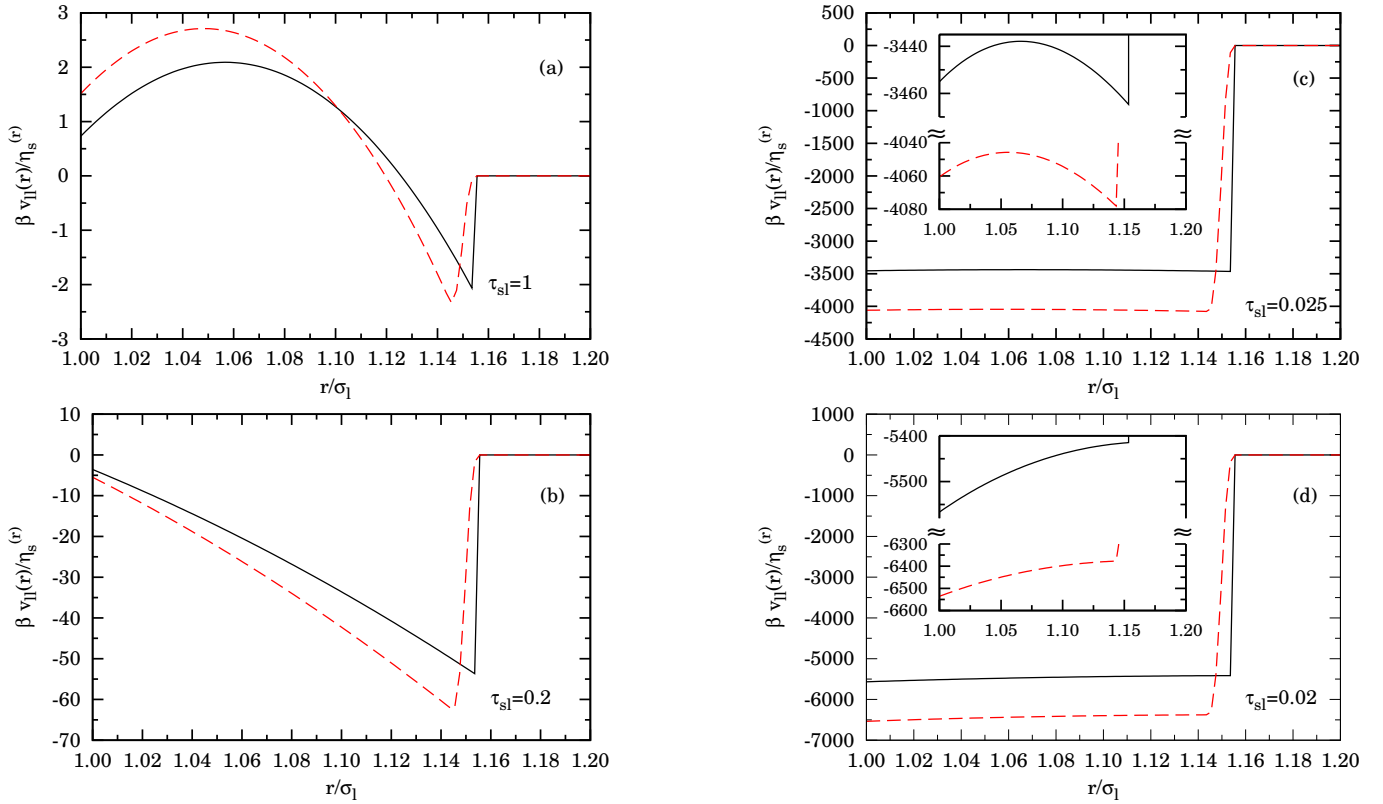


FIG. 7. Plot of $\psi(r) \equiv \beta v_{II}(r)/\eta_s^{(r)}$ for (a) $\tau_{sl} = 1$, (b) $\tau_{sl} = 0.2$, (c) $\tau_{sl} = 0.025$, and (d) $\tau_{sl} = 0.02$. The solid lines correspond to the SAO model at the threshold value $q = q_0$, while the dashed lines correspond to the SWAO model with $q = q_0 - \xi$, $\Delta_{sl} = \xi/(1+q)$, $\xi = 10^{-2}$. The insets in panels (c) and (d) show magnified views of the curves for $r/\sigma_l < 1 + q_0$.

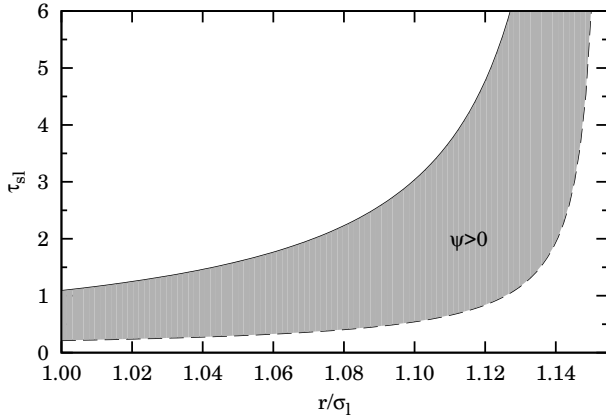


FIG. 8. Plane τ_{sl} vs r showing the region where the effective pair potential in the SAO model for the threshold value $q = q_0$ takes positive values. Outside the shaded region the potential is negative.

pair potential $v_{II}(r)$ at a packing fraction η_l . Up to second

order in η_l , Eq. (4.20) becomes

$$\eta_s \approx \eta_s^{(r)} \left[1 - \eta_l(1+q)^3 \left(1 - \frac{1}{4\tau_{sl}} \right) - \frac{12\eta_l^2 q^3}{\sigma_l^3} \times \int_{\sigma_l}^{\sigma_l(1+q)} dr r^2 \psi(r) e^{-\eta_s^{(r)} \psi(r)} \right], \quad (4.21)$$

Interestingly, exact effective pair-potential (4.12) can be equivalently obtained from a density expansion of the approximate PY effective potential of the ASHS model described in Sec. III, upon neglecting terms of order higher than linear in η_s and identifying η_s with $\eta_s^{(r)}$, that is correct in the solute infinite dilution limit [see Eq. (4.20)]. This is not a coincidence³¹ because the PY theory gives the exact radial distribution function to first order in density (and therefore it gives the exact effective potential to that order) and the relevant Mayer diagram, containing only one solvent particle, is the same whether the mixture is additive or not.

The three terms appearing in Eq. (4.13) bear a particularly simple and instructive physical interpretation. The first term, $\psi_d(r)$, [see Eqs. (4.14) and (4.18)] is the conventional AO effective potential.¹⁶ If $r < \sigma_l(1+q)$, no solvent particles fit in the line joining the centers of the two solute particles. This is the typical configuration

of *depletion* when the solute-solvent interactions are of HS type, giving rise to an effective *attraction* between the solutes (with a force decreasing its strength quadratically with increasing distance). Now imagine we switch the stickiness on. Interestingly, this produces two competing effects. Firstly, the solvent particles attached to the outer surfaces of each facing solute tend to *pull* the solutes apart, producing an effective solute-solute *repulsion* with a constant force strength. This is represented by the “pulling” term $\psi_p(r)$ [see Eqs. (4.15) and (4.19)]. Secondly, the solvent particles attached to *both* facing solutes (the “bridges”) tend to increase *attraction* (with a Coulomb-like force strength decreasing with increasing distance), this bridging effect being represented by the term $\psi_b(r)$ [see Eqs. (4.16) and (4.19)]. These three effects are schematically synthesized in Fig. 6.

It is interesting to remark that the SAO model can be easily extended by replacing the solute-solvent sticky surface by a finite-width (Δ_{sl}) SW interaction. The resulting SWAO model is worked out in Appendix D. In this case, the condition for an exact reduction of the effective solute interaction to pairwise terms is $q(1 + \Delta_{sl}) + \Delta_{sl} < q_0$.

The interplay of the three contributions to $\psi(r)$ gives rise to interesting transitions in the shape of the depletion potential, as illustrated in Fig. 7 for the SAO and SWAO models. Let us comment the curves corresponding to the SAO model. For relatively weak stickiness, $\tau_{sl}^{-1} < \tau_-^{-1} \equiv 24(1 - \sqrt{1 - q - q^2/2})/(1 + q)^2$, the pulling effect dominates over the bridging effect for all distances but is dominated by the depletion effect, except for distances close to $r = \sigma_l(1 + q)$. Consequently, the effective potential is attractive near $r = \sigma_l$ and repulsive near $r = \sigma_l(1 + q)$, as happens in Fig. 7(a). Next, in the intermediate regime $\tau_-^{-1} < \tau_{sl}^{-1} < \tau_+^{-1} \equiv 24(1 + \sqrt{1 - q - q^2/2})/(1 + q)^2$ the pulling effect dominates for all distances and the potential is purely repulsive, except for the discontinuous jump at $r = \sigma_l(1 + q)$. This is represented by the case of Fig. 7(b). In the strong stickiness regime $\tau_+^{-1} < \tau_{sl}^{-1} < 48$ the depletion effect is practically irrelevant and the pulling effect is dominated by the bridging one, except in the region $r \lesssim \sigma_l(1 + q)$. As a consequence, the effective potential is *slightly* attractive near $r = \sigma_l$ and *slightly* repulsive near $r = \sigma_l(1 + q)$, as happens in Fig. 7(c). Finally, for very strong stickiness ($\tau_{sl}^{-1} > 48$) the bridging dominates over the pulling for all distances and the potential is purely attractive. This is the case displayed in Fig. 7(d). Those features are essentially preserved in the case of the SWAO model, except that the jump at $r = \sigma_l(1 + q)$ is replaced by a rapid (but continuous) increase of the potential between $r = \sigma_l(1 + q)$ and $r = \sigma_l(1 + q)(1 + \Delta_{sl})$.

From Eqs. (4.14)–(4.19) it is easy to see that in the SAO model the effective potential and force are positive if

$$\frac{6\hat{r} - \sqrt{6\hat{r}(5\hat{r} - 2)}}{24\hat{r}(1 - \hat{r})(2 + \hat{r})} \leq \tau_{sl} \leq \frac{6\hat{r} + \sqrt{6\hat{r}(5\hat{r} - 2)}}{24\hat{r}(1 - \hat{r})(2 + \hat{r})} \quad (4.22)$$

and

$$\frac{2\hat{r} - \sqrt{2(3\hat{r}^2 - 1)}}{24\hat{r}(1 - \hat{r}^2)} \leq \tau_{sl} \leq \frac{2\hat{r} + \sqrt{2(3\hat{r}^2 - 1)}}{24\hat{r}(1 - \hat{r}^2)}, \quad (4.23)$$

respectively, where $\hat{r} \equiv r/[\sigma_l(1 + q)]$. Figure 8 shows the region in the plane τ_{sl} vs r where $\psi(r) > 0$ for the threshold value $q = q_0$.

As can be seen from Figs. 7(c) and 7(d), the effective potential in the regime of strong stickiness clearly resembles that of a SW potential of width $q\sigma_l$ and depth $\beta\epsilon = \eta_s^{(r)}|\psi(\sigma_l(1 + q))| = \eta_s^{(r)}(1 + q^{-1})^3/192\tau_{sl}^2$. In this case, the effective phase behavior of an equivalent SW fluid would suggest that, for a given $q < q_0$ and a sufficiently small τ_{sl} , we have the appearance of just one lower critical point ($\eta_s^{(r)c}, \eta_l^c$) and the instability region does not close itself again at $\eta_s^{(r)} > \eta_s^{(r)c}$. This is a scenario quite different from the one in the model ASHS, where we found at least one closed island with a lower and an upper critical point (see Sec. III A). It would then be sufficient to switch on a hard-core repulsion (with $\sigma_{ss} = \sigma_s$) among the solvent particles to have a closed spinodal. Along similar lines, it is also interesting to observe that the threshold packing fraction η_s^* defined in Sec. I clearly diverges in the SAO model because the solvent particles can freely overlap.

V. THE NORO-FRENKEL CRITICALITY CRITERION

In 2000, Noro and Frenkel (NF)²⁵ argued that the reduced second virial coefficient B_2/B_2^{HS} , rather than the range and the strength of the attractive interactions, could be the most convenient quantity to estimate the location of the critical point for a wealth of different colloidal suspensions. Their criticality criterion for particles with variable range attractions,²⁵ complemented by the simulation value of the critical temperature obtained in Ref. 37 for the SHS model, yields $B_2/B_2^{\text{HS}} \simeq -1.21$.

In this section we apply the NF criterion to the two models discussed before: the ASHS model (see Sec. III) and the SAO model (see Sec. IV). In both cases, if $v_{ll}(r)$ is the effective solute-solute pair potential, the associated second virial coefficient B_2^{eff} is given by

$$\frac{B_2^{\text{eff}}}{B_2^{\text{HS}}} = 1 - \frac{3}{\sigma_l^3} \int_{\sigma_l}^{\infty} dr r^2 \left[e^{-\beta v_{ll}(r)} - 1 \right], \quad (5.1)$$

where $B_2^{\text{HS}} = 2\pi\sigma_l^3/3$ is the virial coefficient for HSs of diameter σ_l . Paradoxically, while the explicit PY expression of $\beta v_{ll}(r)$ in the ASHS model is rather cumbersome (see Appendix B), its associated second virial coefficient B_2^{eff} is much easier to obtain thanks to properties of the Laplace representation. The result can be found in Eq. (B16). In contrast, in the SAO model the exact expression of $\beta v_{ll}(r)$ is very simple [see Eqs. (4.12)–(4.16)] but the computation of B_2^{eff} needs to be done numerically.

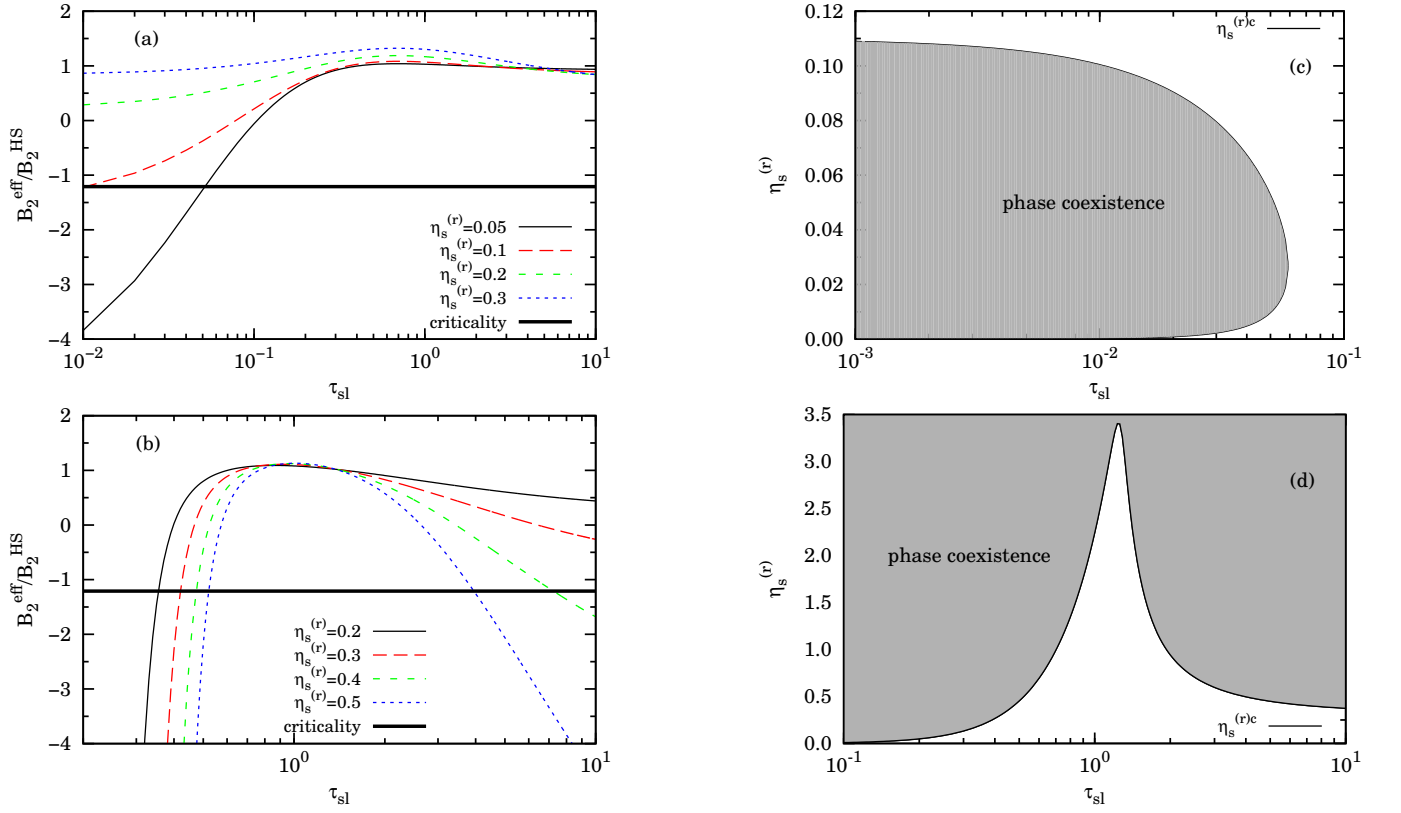


FIG. 9. Second effective virial coefficient as a function of τ_{sl} for $q = q_0$ and several values of $\eta_s^{(r)}$ for (a) ASHS and (b) SAO models. The thick horizontal line corresponds to the NF criticality criterion $B_2^{\text{eff}}/B_2^{\text{HS}} = -1.21$. Panels (c) and (d) show the dependence of the critical value $\eta_s^{(r)} = \eta_s^{(r)c}$ (according to the NF criterion) as a function of τ_{sl} for the ASHS and SAO models, respectively. Note that a logarithmic scale is used on the abscissas.

It is particularly instructive to observe that the NF criterion confirms the very different critical behavior between the ASHS model ($\sigma_{ss}/\sigma_s = 1$) and the SAO model ($\sigma_{ss}/\sigma_s = 0$). In Figs. 9(a) and 9(b) we compare the second effective virial coefficients for the two models as functions of τ_{sl} for $q = q_0$ and several values of $\eta_s^{(r)}$. Here we have identified $\eta_s \rightarrow \eta_s^{(r)}$ in the ASHS case, in consistency with the fact that the effective potential is derived in the infinite solute dilution limit. The loci of points in the plane $\eta_s^{(r)}$ vs τ_{sl} where $B_2^{\text{eff}}/B_2^{\text{HS}} = -1.21$ are displayed in Figs. 9(c) and 9(d). Inside the shaded regions one has $B_2^{\text{eff}}/B_2^{\text{HS}} < -1.21$ and thus phase coexistence is possible, according to the NF criterion.

As we already knew from the results of Sec. III A, Figs. 9(a) and 9(c) show criticality in the ASHS model only for sufficiently small τ_{sl} and $\eta_s^{(r)}$. On the other hand, the scenario present in the SAO model is completely different. It is easy to check that a critical point in the pure AO model ($\tau_{sl} \rightarrow \infty$) exists only, according to the NF criterion, if $\eta_s^{(r)} \gtrsim 0.318$. However, the presence of stickiness (finite τ_{sl}) dramatically changes the picture. For any $\eta_s^{(r)}$, there exists a critical point if τ_{sl} is small enough. Beyond a certain threshold value, criticality abruptly disappears and then (only if $\eta_s^{(r)} \gtrsim 0.318$) it *re-enters* at a sufficiently

large value of τ_{sl} . Thus, if $\eta_s^{(r)} \gtrsim 0.318$ there exists a window of values of τ_{sl} where no phase separation is possible. Note that values of $\eta_s^{(r)} > 1$, as displayed in Fig. 9(d), are not unphysical in the SAO model since the reservoir consists in an ideal gas of noninteracting small particles.

It must be remarked that the bridging and pulling effects are more important in the nonadditive SAO case than in the additive ASHS one, since in the latter the mutual exclusion of solvent particles interferes with their ability to attach to the solutes. As illustrated in Fig. 9, this leads to paramount differences in the critical behavior of the two extreme models. For intermediate NASHS models with $0 < \sigma_{ss}/\sigma_s < 1$ (see Fig. 3) a transition from Figs. 9(b) and 9(d) to Figs. 9(a) and 9(c), respectively, can be expected as the excluded volume among the solvent spheres is gradually increased.

Note also that in the ASHS model [Fig. 9(a)] the results are approximate (PY) and the solute concentration is zero. On the contrary, in the SAO model [Fig. 9(b)], the results are exact and valid for any finite solute and solvent concentrations. While both models coincide in the limit of vanishing solvent concentration, in practice this equivalence requires extremely small values of $\eta_s^{(r)}$. For instance, at $\eta_s^{(r)} = 10^{-5}$ both values of B_2^{eff} differ by

nearly 2%.

VI. PERTURBATION THEORY FOR THE SAO MODEL

From Sec. V we conclude that the “hidden” fluid-fluid phase separation observed by Dijkstra et al.¹⁶ in their study of the AO model could be stabilized by adding adhesion, as in our SAO model. This can be quantified more precisely using a first-order thermodynamic perturbation theory.³⁹

Assuming the HS fluid as reference system, we can write the Helmholtz free energy per particle of the effective solute system as

$$\frac{\beta F^{\text{eff}}}{N_l} = \frac{\beta F_{\text{HS}}}{N_l} + 12\eta_l \eta_s^{(r)} \int_{\sigma_l}^{\sigma_l(1+q)} dr r^2 \psi(r) g_{\text{HS}}(r|\eta_l), \quad (6.1)$$

where $\beta F_{\text{HS}}/N_l = (4\eta_l - 3\eta_l^2)/(1 - \eta_l)^2 + \ln(\eta_l) + \text{const}$ is the Carnahan–Starling⁴¹ HS expression, $\psi(r)$ is given by Eqs. (4.13)–(4.16), and g_{HS} is the HS radial distribution function in the PY approximation⁴², which in the interval $\sigma_l < r < \sigma_l(1+q) < 2$ can be written as

$$g_{\text{HS}}(r|\eta_l) = \sum_{n=1}^3 \lim_{t \rightarrow t_n(\eta_l)} \frac{[t - t_n(\eta_l)] t L(t|\eta_l) e^{t(r-1)}}{S(t|\eta_l) r}, \quad (6.2)$$

where we are measuring lengths in units of σ_l ,

$$S(t|\eta_l) = (1 - \eta_l)^2 t^3 + 6\eta_l(1 - \eta_l)t^2 + 18\eta_l^2 t - 12\eta_l(1 + 2\eta_l), \quad (6.3)$$

$$L(t|\eta_l) = (1 + \eta_l/2)t + 1 + 2\eta_l, \quad (6.4)$$

and $t_n(\eta_l)$ ($n = 1, 2, 3$) are the zeros of $S(t|\eta_l)$. The first-order Helmholtz free energy of Eq. (6.1) can thus be calculated analytically.

The compressibility factor $Z = \beta p/\rho$ and chemical potential μ are then found through

$$Z^{\text{eff}} = \eta_l \left. \frac{\partial(\beta F^{\text{eff}}/N_l)}{\partial \eta_l} \right|_{\eta_s^{(r)}}, \quad (6.5)$$

$$\beta \mu^{\text{eff}} = Z^{\text{eff}} + \frac{\beta F^{\text{eff}}}{N_l}. \quad (6.6)$$

The critical point $(\eta_s^{(r)c}, \eta_l^c)$ is determined by numerically solving the following set of equations:

$$\left. \frac{\partial(\eta_l Z^{\text{eff}})}{\partial \eta_l} \right|_{\eta_s^{(r)c}, \eta_l^c} = 0, \quad (6.7)$$

$$\left. \frac{\partial^2(\eta_l Z^{\text{eff}})}{\partial \eta_l^2} \right|_{\eta_s^{(r)c}, \eta_l^c} = 0. \quad (6.8)$$

In Fig. 10 we show the critical point $(\eta_s^{(r)c}, \eta_l^c)$ for the fluid-fluid coexistence in the SAO model at the threshold value $q = q_0$ as a function of τ_{sl} . The figure confirms the scenario predicted in Sec. V from the NF criterion. In fact, Fig. 10 shows a relevant mutual consistency between

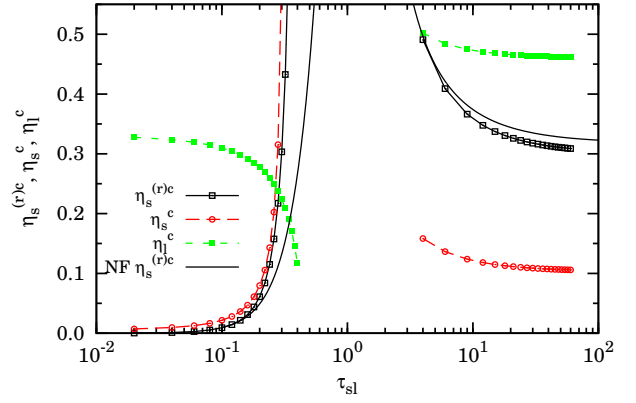


FIG. 10. Critical point for the fluid-fluid coexistence in the SAO model for $q = q_0$ as a function of τ_{sl} . The lines with symbols are obtained from perturbation theory, while the solid line corresponds to the NF criterion [see Fig. 9(d)]. A logarithmic scale is used on the abscissa. Equation (4.21) is used for the conversion between the reservoir and the solvent densities.

the curves for $\eta_s^{(r)c}$ as obtained from both independent approaches. There is a range of adhesion for which there is no criticality. For high adhesions (small τ_{sl}) we have phase coexistence in the region of low $\eta_s^{(r)}$ region, while for low adhesions (large τ_{sl}) the criticality exists in the region of high $\eta_s^{(r)}$. Of course, we expect a breakdown of the perturbation theory treatment as soon as stickiness becomes too strong. Also, as soon as $q > q_0$ we are neglecting three-body (and higher) terms.

VII. CONCLUSIONS

In this paper, we have studied two complementary models of a binary mixture of (small) solvent and (large) solute particles, where in both cases unlike particles experience an attractive adhesion interaction of Baxter’s type.⁷ We studied the derivation of an effective solute-solute pair-potential for the two models in the regime of large size asymmetry ($q = \sigma_s/\sigma_l \ll 1$) and discussed analogies and differences of the corresponding phase behaviors, as obtained from the resulting effective one-component fluid.

In the first model, that we dubbed ASHS, both solute-solute and solvent-solvent particles interact as HSs and the reduction to an effective one-component fluid can be carried out only approximately via a small solute density expansion. By contrast, this model admits an exact analytical solution within the PY approximation. In the limit of vanishing solute-solvent adhesive attraction, this model reduces to the usual AHS binary mixture, that is known not to display any phase separation within the PY approximation. This might, however, be ascribed to the limitations of the PY closure, as other more sophisticated theories, as well as numerical simulations, support

the existence of phase separation, albeit metastable with respect to freezing, at sufficiently large concentrations and size asymmetry (in this context, nevertheless, see Ref. 43). In this case, our analysis of the ASHS model confirms previous findings of a similar study by Chen et al.¹¹ in predicting a closed region in the (η_s, η_l) plane where phase separation occurs.

While the ASHS model has been around for some time,¹² the second model (denoted as SAO) is, to the best of our knowledge, new. In this case, solvent particles behave as an ideal gas within each other—but still they experience a SHS interaction with the solutes. In the limit of no adhesion between solute and solvent, this model reduces to the well-known AO one, and we have extended the analysis performed by Dijkstra et al.¹⁷ to the present case. As in the AO case, even in the SAO case the solvent degrees of freedom can be traced out exactly above a well defined size asymmetry (that is, below a critical value q_0 of the size ratio q), so that the resulting effective one-component pair potential is *exact*. By contrast, it is not possible in this case to obtain an exact analytical solution of the binary problem (not even within the PY approximation), so we resorted to study a first-order thermodynamic perturbation theory of the corresponding exact effective solute-solute pair potential.

In both models, effective potentials can be explained in terms of “pulling” and “bridging” effects in addition to the usual “depletion” mechanism. In the SAO case, the analytical expressions of the effective potential derived in Eqs. (4.12)–(4.16) allow for an interesting direct physical interpretation. The pulling effect is represented by the term proportional to τ_{sl}^{-1} [see Eq. (4.15)], as the same (solvent) particle must be in contact with one of the solutes and outside the exclusion volume of the other solute. On the other hand, the bridging effect is represented by the term proportional to τ_{sl}^{-2} [see Eq. (4.16)], as the same (solvent) particle must be in contact with both solute particles. These effects are present in both models, but they are more important in the SAO case than in the ASHS case, since in the latter, the mutual exclusion of solvent particles interferes with their ability to be attached to the solutes. In fact, the situation sketched in Fig. 2(d) is inhibited in the SAO model, as represented by Fig. 9(d), which shows always phase coexistence at increasing $\eta_s^{(r)}$ for any fixed τ_{sl} .

The derivation of the exact SAO effective potential has allowed us to clearly assess the dramatic influence of solute-solvent attraction on the conventional AO depletion potential. This complements a recent study,⁴⁴ where softness in the solute-solvent repulsion was seen to strongly enhance the depletion mechanism.

Leaving aside the issue of the metastability with respect to the fluid-solid transition, the resulting picture confirms the significant impact of nonadditivity on the fluid-fluid phase diagram, as synthesized by Fig. 9. Within the NF criticality criterion, the SAO model is expected to display a reentrant phase transition in terms of τ_{sl} , whereas the ASHS model is not. On the other hand,

the results for the ASHS model are compatible with a reentrant phase transition in terms of η_s not observed in the SAO model. A first-order perturbation theory on the SAO model confirms this picture.

Our findings nicely confirm and complement those by Chen et al.,¹¹ but extend them to encompass a *direct* connection with the AO original model, that was missing in the above study, thus paving the way to a more direct interpretation of the experimental results reported in Refs. 8 and 9.

While direct numerical simulations of binary mixtures with large size asymmetries are notoriously difficult, it would be interesting to study with numerical experiments whether adhesion gives rise to the appearance of a metastable fluid-fluid coexistence at large solvent densities for the ASHS model with large q and for the SAO model with very small q . In addition, they open a number of interesting perspectives for future studies. Even without resorting to a direct numerical simulation calculations, a number of different theoretical approaches can be exploited to make further progresses.

As the attraction between the unlike spheres vanishes ($\tau_{sl} \rightarrow \infty$), the PY solution of the ASHS model reduces to the well-known PY solution for a binary AHS mixture,⁴⁵ which does not show phase separation for any size ratio, in spite of the possible depletion interactions. As said above, this seems to be an artifact of the PY approximation, as shown by numerical simulations of the (approximate) effective one-component fluid¹⁶ and by numerical solutions of the Rogers and Young (RY) closure.⁴⁶ Thus, one possibility would be to use the RY closure on a binary mixture with HS interactions between like particles and a short-range SW attraction (in the regimes where this can be considered sticky-like^{47,48}) between unlike spheres. Work along these lines is in progress and will be reported elsewhere.

Another possibility would be to consider a binary ASHS mixture with HS interactions between small spheres, weak SHS interactions between the large spheres, and stronger SHS interactions between small and big spheres. This two-component model (which is known to be free from the thermodynamic inconsistency affecting the one-component model⁴⁹) could be solved rather easily within the PY approximation, as done for instance by Zaccarelli et al.⁵⁰

Finally, it would be nice to extend the study reported here for the ASHS and SAO models to a more general NASHS model where one could tune the solvent-solvent diameter from zero (SAO model) to the additive value (ASHS model), thus encompassing both models into an unified framework. MC simulations for a binary ASHS mixture have been performed by Jamnik,⁵¹ but not for the determination of the phase diagram, which has been studied for the one-component SHS fluid by Miller and Frenkel.^{37,52} To the best of our knowledge, no numerical experiment has ever been tried on the NASHS binary mixture.

ACKNOWLEDGMENTS

A.G. gratefully acknowledges support from PRIN-MIUR 2010-2011 project (contract 2010LKE4CC). The research of A.S. has been partially supported by the Spanish Government through Grant No. FIS2013-42840-P and by the Regional Government of Extremadura (Spain) through Grant No. GR15104 (partially financed by ERDF funds).

Appendix A: A simple geometrical argument related to Fig. 2

We first estimate how many small spheres of diameter σ_s are necessary to cover the surface of a large sphere of diameter σ_l . Assuming $q = \sigma_s/\sigma_l \ll 1$, the small spheres will be distributed on the large sphere surface approximately with a hexagonal packing corresponding to an *area* fraction $\eta_{\text{hex}} = \pi/2\sqrt{3} \approx 0.907$. Thus, $\eta_{\text{hex}} = \phi a/A$, where ϕ is the number of the adsorbed small spheres, $a = (\pi/4)\sigma_s^2$ is the area of the projected disk associated with each solvent sphere, and $A = \pi\sigma_l^2$ is the surface area of the solute particle. Therefore,

$$\phi = \eta_{\text{hex}} \frac{A}{a} = \frac{2\pi}{\sqrt{3}} q^{-2}. \quad (\text{A1})$$

The critical volume fraction η_s^* at which all large colloidal spheres, distributed with a volume fraction $\eta_l = (\pi/6)\rho_l\sigma_l^3$, can be covered is

$$\eta_s^* = \eta_l q^3 \phi \quad (\text{A2})$$

and this leads to the expression reported in Sec. I.

Appendix B: Analytical PY expressions for the ASHS model in the limit $x_l \rightarrow 0$

The Rational-Function Approximation (RFA) methodology^{15,31,53} is known to give access to analytical formulae of the PY solution for the ASHS model.^{7,12,28} In this Appendix we assume the infinite dilution limit for the solutes ($x_l \rightarrow 0$).

According to Eq. (36) of Ref. 31, the Laplace transform $G_{ll}(s) = \int_0^\infty dr e^{-sr} r g_{ll}(r)$ of $rg_{ll}(r)$ is, in the limit $x_l \rightarrow 0$,

$$G_{ll}(s) = \frac{e^{-s}}{s^2} \left[L_{ll}(s) + L_{ls}(s) \frac{A_{sl}(s)}{1 - A_{ss}(s)} \right], \quad (\text{B1})$$

where $\sigma_l = 1$ has been chosen as length unit and¹⁵

$$L_{ll}(s) = L_{ll}^{(0)} + L_{ll}^{(1)} s, \quad (\text{B2})$$

$$L_{ls}(s) = L_{ls}^{(0)} + L_{ls}^{(1)} s + L_{ls}^{(2)} s^2, \quad (\text{B3})$$

$$A_{sl}(s) = 12\eta_s \left[\phi_2(qs) L_{sl}^{(0)} + \frac{\phi_1(qs)}{q} L_{sl}^{(1)} + \frac{\phi_0(qs)}{q^2} L_{sl}^{(2)} \right], \quad (\text{B4})$$

$$A_{ss}(s) = 12\eta_s \left[\phi_2(qs) L_{ss}^{(0)} + \frac{\phi_1(qs)}{q} L_{ss}^{(1)} \right]. \quad (\text{B5})$$

Here, $\phi_n(x) \equiv -x^{-(n+1)} \left[e^{-x} - \sum_{j=0}^n (-x)^j / j! \right]$. The coefficients $L_{\alpha\gamma}^{(k)}$ are given by¹⁵

$$L_{ll}^{(0)} = L_{sl}^{(0)} = \frac{1 - (12\eta_s/q^2) L_{sl}^{(2)}}{1 - \eta_s} + \frac{3\eta_s}{q(1 - \eta_s)^2}, \quad (\text{B6})$$

$$L_{ls}^{(0)} = L_{ss}^{(0)} = \frac{1}{1 - \eta_s} + \frac{3\eta_s}{(1 - \eta_s)^2}, \quad (\text{B7})$$

$$L_{ll}^{(1)} = \frac{1 - (6\eta_s/q^2) L_{sl}^{(2)}}{1 - \eta_s} + \frac{3\eta_s}{2q(1 - \eta_s)^2}, \quad (\text{B8})$$

$$L_{sl}^{(1)} = \frac{1 + q - (12\eta_s/q) L_{sl}^{(2)}}{2(1 - \eta_s)} + \frac{3\eta_s}{2(1 - \eta_s)^2}, \quad (\text{B9})$$

$$L_{ls}^{(1)} = \frac{1 + q}{2(1 - \eta_s)} + \frac{3\eta_s}{2(1 - \eta_s)^2}, \quad (\text{B10})$$

$$L_{ss}^{(1)} = q \frac{1 + \eta/2}{(1 - \eta)^2}, \quad (\text{B11})$$

$$L_{ls}^{(2)} = L_{sl}^{(2)} = \frac{1}{12} \frac{1 + q + \frac{3\eta_s}{1 - \eta_s}}{4\tau_{sl} \frac{1 - \eta_s}{1 + q} + \eta_s/q}. \quad (\text{B12})$$

This closes the determination of $G_{ll}(s)$ for given values of η_s , q , and τ_{sl} . Then, by numerical inverse transform one can easily obtain $g_{ll}(r)$. On the other hand, pure analytical expressions are also possible for the different layers $1 < r < 1 + q$, $1 + q < r < 1 + 2q$, $1 + 2q < r < 1 + 3q$, ... The trick consists in formally attaching a bookkeeping factor ε to any exponential in $G_{ll}(s)$. Then, by expanding in powers of ε we can write

$$G_{ll}(s) = \sum_{n=0}^{\infty} e^{-(1+nq)s} \Gamma_n(s), \quad (\text{B13})$$

where we have made $\varepsilon = 1$. From Eq. (B13) we get

$$g_{ll}(r) = \frac{1}{r} \sum_{n=0}^{\infty} \Theta(r - 1 - nq) \gamma_n(r - 1 - nq), \quad (\text{B14})$$

where $\gamma_n(r)$ is the inverse Laplace transform of $\Gamma_n(s)$. The functions $\gamma_n(r)$ can then be expressed in terms of the three roots of a cubic equation, analogously to the case of Eq. (6.2). Therefore, if we are only interested in

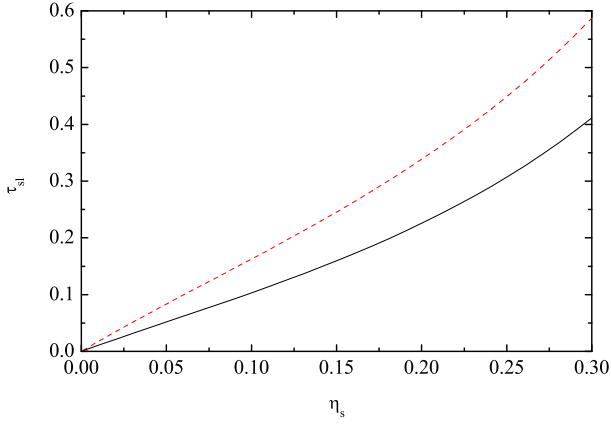


FIG. 11. Loci in the plane τ_{sl} vs η_s where the PY approximation predicts $g_{ll}(r) = 0$ at $r = (1+q)^+$ for $q = 0.12$ (upper curve) and $q = q_0$ (lower curve). The radial distribution function $g_{ll}(r)$ is not positive definite below each curve.

the interval $1 \leq r \leq 1+kq$, we just need to keep the first k terms in the sum of Eq. (B14).

From a practical point of view, it is sufficient to determine $g_{ll}(r)$ in the interval $1 \leq r \leq 1+3q$, in which case only $\gamma_0(r)$, $\gamma_1(r)$, and $\gamma_2(r)$ are needed. Their analyti-

cal expressions are easily obtained with a computational software program but are too lengthy to be reproduced here. In general, $\gamma_1(0) \neq 0$, what implies a jump discontinuity of $g_{ll}(r)$ at $r = 1+q$,

$$\begin{aligned} \delta g_{ll} &\equiv g_{ll}((1+q)^-) - g_{ll}((1+q)^+) = -\frac{\gamma_1(0)}{1+q} \\ &= \frac{(1+q)\eta_s [1+q+(2-q)\eta_s]^2}{12q(1-\eta_s)^2 [(1+q)\eta_s + 4q\tau_{sl}(1-\eta_s)]^2}. \end{aligned} \quad (\text{B15})$$

Note that $r = 1+q$ is the threshold distance beyond which no bridges are possible (see Fig. 2). This is clearly reflected by a strong decrease of $g_{ll}(r)$ when going from $r = (1+q)^-$ (bridges are possible) to $r = (1+q)^+$ (no bridging effect). This physical phenomenon can give rise, as an artifact of the PY approximation, to a negative value of $g_{ll}(r)$ at $r = (1+q)^+$ if η_s is sufficiently large or τ_{sl} is sufficiently small. This is illustrated in Fig. 11 for $q = 0.12$ and $q = q_0$.

Once $g_{ll}(r)$ is known, Eq. (3.2) gives the pair potential $v_{ll}(r)$ in the PY approximation, as depicted in Fig. 5. The effective second virial coefficient can also be determined analytically as follows:

$$\begin{aligned} B_2^{\text{eff}} &= -2\pi \int_0^\infty dr r^2 [g_{ll}(r) - 1] = 2\pi \lim_{s \rightarrow 0} \frac{\partial}{\partial s} [G_{ll}(s) - s^{-2}] \\ &= \frac{\pi}{12(1+2\eta_s)^2} \left\{ 8 + (20 - 15q - 6q^2 - q^3)\eta_s + 2(4 - 6q + 3q^2 + q^3)\eta_s^2 - q^3\eta_s^3 \right. \\ &\quad + \frac{2(1+q)\eta_s(1+q+2\eta_s-q\eta_s) [6(1+2\eta_s) + q^2(1-\eta_s)^2 + 2q(1-\eta_s)(2+\eta_s)]}{(1-\eta_s)[(1+q)\eta_s + 4q\tau_{sl}(1-\eta_s)]} \\ &\quad \left. - \frac{(1+q)^2\eta_s(1+q+2\eta_s-q\eta_s)^2(2+q+4\eta_s-q\eta_s)}{(1-\eta_s)[(1+q)\eta_s + 4q\tau_{sl}(1-\eta_s)]^2} \right\}. \end{aligned} \quad (\text{B16})$$

Appendix C: Derivation of the relationship between η_s , η_l , and $\eta_s^{(r)}$ in the SAO model

In the semi-grand-canonical ensemble (z_s, N_l, V, T) the average number of small particles can be obtained from the associated thermodynamic potential \mathcal{F} as

$$\langle N_s \rangle_{z_s, N_l} = -z_s \frac{\partial \beta \mathcal{F}}{\partial z_s}. \quad (\text{C1})$$

Now, from Eq. (4.2) and the equality $U_{ll}^{\text{eff}} = U_{ll} + \Omega$, we can write

$$e^{-\beta \mathcal{F}} = \langle e^{-\beta \Omega} \rangle_{N_l} \frac{\int d\mathbf{r}^{N_l} e^{-\beta U_{ll}}}{N_l! \Lambda_l^{3N_l}}, \quad (\text{C2})$$

where

$$\langle \dots \rangle_{N_l} = \frac{\int d\mathbf{r}^{N_l} \dots e^{-\beta U_{ll}}}{\int d\mathbf{r}^{N_l} e^{-\beta U_{ll}}} \quad (\text{C3})$$

denotes a canonical average over the bare solutes. Then, taking into account that $\Omega \propto z_s$, Eq. (C1) reduces to

$$\langle N_s \rangle_{z_s, N_l} = -\frac{\langle e^{-\beta \Omega} \beta \Omega \rangle_{N_l}}{\langle e^{-\beta \Omega} \rangle_{N_l}}. \quad (\text{C4})$$

Next, if $q < q_0$, $\Omega = \Omega_0 + \Omega_1 + \Omega_2$, so that

$$\langle N_s \rangle_{z_s, N_l} = -\beta \Omega_0 - \beta \Omega_1 - \frac{\langle e^{-\beta \Omega_2} \beta \Omega_2 \rangle_{N_l}}{\langle e^{-\beta \Omega_2} \rangle_{N_l}}. \quad (\text{C5})$$

Note that the last term on the right-hand side can be

rewritten as

$$\frac{\langle e^{-\beta\Omega_2} \beta\Omega_2 \rangle_{N_l}}{\langle e^{-\beta\Omega_2} \rangle_{N_l}} = \frac{\rho_l^2}{2} V \int d\mathbf{r} \beta v_{ll}(r) g_{\text{eff}}(r | \eta_l, \eta_s^{(r)}), \quad (\text{C6})$$

where

$$g_{\text{eff}}(r_{12}^{(l)} | \eta_l, \eta_s^{(r)}) = \frac{V^2 \int d\mathbf{r}_3^{(l)} \dots \int d\mathbf{r}_{N_l}^{(l)} e^{-\beta U_{ll}^{\text{eff}}}}{\int d\mathbf{r}^{N_l} e^{-\beta U_{ll}^{\text{eff}}}} \quad (\text{C7})$$

and we have taken into account that $N_l(N_l - 1) \simeq N_l^2$ in the thermodynamic limit. Finally, applying Eqs. (4.7), (4.11), and (C6) in Eq. (C5), it is easy to obtain Eq. (4.20).

The first two terms on the right-hand side of Eq. (4.20) can also be obtained from the canonical ensemble (N_s, N_l, V, T) . Up to the level of the second virial coefficient, the free energy F is

$$\frac{\beta F}{V} = \rho_s \ln(\rho_s \Lambda_s^3) + \rho_l \ln(\rho_l \Lambda_l^3) - \rho_s - \rho_l + \frac{2\pi}{3} \rho_l^2 + 2B_{sl} \rho_s \rho_l + \mathcal{O}(\rho^3), \quad (\text{C8})$$

where $B_{sl} = \frac{\pi}{12} \sigma_l^3 (1+q)^3 \left(1 - \frac{1}{4\tau_{sl}}\right)$. The solvent chemical potential is $\mu_s = [\partial(F/V)/\partial\rho_s]_{\rho_l}$, so that

$$z_s \equiv \frac{e^{\beta\mu_s}}{\Lambda_s^3} = \rho_s [1 + 2B_{sl} \rho_l + \mathcal{O}(\rho^2)], \quad (\text{C9})$$

which is consistent with Eq. (4.20).

Appendix D: SWAO model

In the SWAO model Eq. (2.10) is replaced by

$$f_{sl}(r) = \begin{cases} -1, & r < \sigma_{sl}, \\ e^{\beta\epsilon_{sl}} - 1, & \sigma_{sl} < r < \sigma_{sl}(1 + \Delta_{sl}), \\ 0, & r > \sigma_{sl}(1 + \Delta_{sl}), \end{cases} \quad (\text{D1})$$

where ϵ_{sl} and $\sigma_{sl}\Delta_{sl}$ are the depth and width, respectively, of the attractive well. One can define an effective stickiness parameter⁴⁷ $\tau_{sl}^{-1} = 12(e^{\beta\epsilon_{sl}} - 1)\Delta_{sl}$, so that the SWAO model reduces to the SAO one in the double limit $\epsilon_{sl} \rightarrow \infty$, $\Delta_{sl} \rightarrow 0$ at fixed τ_{sl} .

All the steps in Sec. IV up to Eq. (4.10) are still valid for the SWAO model. However, the condition for having $\Omega_n = 0$ if $n \geq 3$ is not $\sigma_{sl} < \sigma_l(1 + q_0)/2$ (or $q < q_0$) but $\sigma_{sl}(1 + \Delta_{sl}) < \sigma_l(1 + q_0)/2$, what is equivalent to $q(1 + \Delta_{sl}) + \Delta_{sl} < q_0$.

To simplify the expressions, in this appendix we take again $\sigma_l = 1$ as the length unit. Inserting Eq. (D1) into Eq. (4.10), one obtains

$$\beta v_{ll}(r) = \eta_s^{(r)} \begin{cases} \infty, & r < 1, \\ \psi(r), & 1 < r < (1+q)(1+\Delta_{sl}), \\ 0, & r > (1+q)(1+\Delta_{sl}), \end{cases} \quad (\text{D2})$$

where the function $\psi(r)$ can again be decomposed into three terms (depletion+pulling+bridging), as given by Eq. (4.13), except that now

$$\psi_{\text{p}}(r) = \frac{(\tau_{sl}\Delta_{sl})^{-1}}{8\pi q^3} [\mathcal{C}(r_-, 1+q) + \mathcal{C}(r_+, (1+q)(1+\Delta_{sl})) - 2\mathcal{C}(r, 1+q)], \quad (\text{D3})$$

$$\psi_{\text{b}}(r) = -\frac{(\tau_{sl}\Delta_{sl})^{-2}}{96\pi q^3} [\mathcal{C}(r, 1+q) + \mathcal{C}(r, (1+q)(1+\Delta_{sl})) - \mathcal{C}(r_-, 1+q) - \mathcal{C}(r_+, (1+q)(1+\Delta_{sl}))], \quad (\text{D4})$$

where

$$\mathcal{C}(r, a) = \frac{\pi}{3} (a-r)^2 (2a+r) \Theta(a-r) \quad (\text{D5})$$

is the volume of a spherical cap of height $a-r$ in a sphere of radius a and

$$r_{\pm} \equiv r \pm \frac{(1+q)^2}{2r} \Delta_{sl} \left(1 + \frac{\Delta_{sl}}{2}\right). \quad (\text{D6})$$

The depletion term is still given by Eq. (4.14), i.e., $\psi_{\text{d}}(r) = -(3/2\pi q^3)\mathcal{C}(r, 1+q)$.

The ranges of the contributions $\psi_{\text{d}}(r)$, $\psi_{\text{p}}(r)$, and $\psi_{\text{b}}(r)$ are $1+q$, $(1+q)(1+\Delta_{sl}/2)$, and $(1+q)(1+\Delta_{sl})$, respectively. It can be easily verified that in the sticky limit $\Delta_{sl} \rightarrow 0$ the potential of Eq. (D2) reduces to the one of Eq. (4.12). One can also verify that the jump discontinuity at $r = 2\sigma_{sl} = 1+q$ of the SAO model disappears in the SWAO one, which is everywhere continuous.

- ¹S. Asakura and F. Oosawa, J. Chem. Phys. **22**, 1255 (1954).
- ²Usually, when talking about the AO model one refers to a colloid-polymer mixture where the depletants are linear homopolymers of radius of gyration $\sigma_s/2$ in a good solvent. After tracing out the monomer degrees of freedom and replacing each chain with a particle at its center of mass, the homopolymers can be considered, to a first level of approximation, as noninteracting among themselves but unable to penetrate a sphere of diameter $\sigma_l + \sigma_s$ around each colloidal particle. In this work, however, we will rather talk about a solvent-solute mixture.
- ³L. Sapir and D. Harries, J. Phys. Chem. Lett. **5**, 1061 (2014).
- ⁴L. Sapir and D. Harries, Curr. Opin. Colloid In. **20**, 3 (2015).
- ⁵C. Bechinger, D. Rudhardt, P. Leiderer, R. Roth, and S. Dietrich, Phys. Rev. Lett. **83**, 3960 (1999).
- ⁶Y. C. Kim and J. Mittal, Phys. Rev. Lett. **110**, 208102 (2013).
- ⁷R. J. Baxter, J. Chem. Phys. **49**, 2770 (1968).
- ⁸C. Zhao, G. Yuan, D. Jia, and C. C. Han, Soft Matter **8**, 7036 (2012).
- ⁹C. Zhao, G. Yuan, and C. C. Han, Macromolecules **45**, 9468 (2012).
- ¹⁰R. Fantoni, J. W. O. Salari, and B. Klumperman, Phys. Rev. E **85**, 061404 (2012).
- ¹¹J. Chen, S. R. Kline, and Y. Liu, J. Chem. Phys. **142**, 084904 (2015); Erratum, *ibid.* **142**, 149901 (2015).
- ¹²R. Fantoni, D. Gazzillo, and A. Giacometti, Phys. Rev. E **72**, 011503 (2005).
- ¹³J. W. Perram and E. R. Smith, Chem. Phys. Lett. **35**, 138 (1975).
- ¹⁴B. Barbo, Chem. Phys. **11**, 357 (1975).
- ¹⁵A. Santos, S. B. Yuste, and M. López de Haro, J. Chem. Phys. **109**, 6814 (1998).
- ¹⁶M. Dijkstra, R. van Roij, and R. Evans, Phys. Rev. E **59**, 5744 (1999).

- ¹⁷M. Dijkstra, J. M. Brader, and R. Evans, *J. Phys.: Condens. Matter* **11**, 10079 (1999).
- ¹⁸K. Binder, P. Virnau, and A. Statt, *J. Chem. Phys.* **141**, 140901 (2014).
- ¹⁹D. J. Ashton and N. B. Wilding, *Phys. Rev. E* **89**, 031301(R) (2014).
- ²⁰D. J. Ashton and N. B. Wilding, *J. Chem. Phys.* **140**, 244118 (2014).
- ²¹A. Santos, M. López de Haro, G. Fiumara, and F. Saija, *J. Chem. Phys.* **142**, 224903 (2015).
- ²²T. Zykova-Timan, *J. Chem. Phys.* **133**, 014705 (2010).
- ²³E. G. Noya, C. Vega, and E. de Miguel, *J. Chem. Phys.* **128**, 154507 (2008).
- ²⁴L. A. Fernández, V. Martín-Mayor, B. Seone, and P. Verrocchio, *Phys. Rev. Lett.* **108**, 165701 (2012).
- ²⁵M. G. Noro and D. Frenkel, *J. Chem. Phys.* **113**, 2941 (2000).
- ²⁶R. Menichetti, A. Pelissetto, G. D. Adamo, and C. Pierleoni, “Integral equation analysis of single-site coarse-grained models for polymercolloid mixtures,” *Mol. Phys.* (published online 2015).
- ²⁷M. Dijkstra, R. van Roij, and R. Evans, *Phys. Rev. Lett.* **82**, 117 (1999).
- ²⁸R. J. Baxter, *J. Chem. Phys.* **52**, 4559 (1970).
- ²⁹B. Barboy and R. Tenne, *Chem. Phys.* **38**, 369 (1979).
- ³⁰D. Gazzillo and A. Giacometti, *J. Chem. Phys.* **120**, 4742 (2004).
- ³¹S. B. Yuste, A. Santos, and M. López de Haro, *J. Chem. Phys.* **128**, 134507 (2008).
- ³²R. Fantoni and A. Santos, *J. Chem. Phys.* **140**, 244513 (2014).
- ³³L. Vega, E. de Miguel, L. F. Rull, G. Jackson, and I. A. McLure, *J. Chem. Phys.* **96**, 2296 (1992).
- ³⁴H. Liu, S. Garde, and S. Kumar, *J. Chem. Phys.* **123**, 174505 (2005).
- ³⁵L. Acedo and A. Santos, *J. Chem. Phys.* **115**, 2805 (2001).
- ³⁶R. Espíndola-Heredia, F. del Río, and A. Malijevský, *J. Chem. Phys.* **130**, 024509 (2009).
- ³⁷M. Miller and D. Frenkel, *J. Chem. Phys.* **121**, 535 (2004).
- ³⁸A. Statt, P. Virnau, and K. Binder, “Crystal nuclei in melts: A Monte Carlo simulation of a model for attractive colloids,” *Mol. Phys.* (published online 2015).
- ³⁹A. P. Gast, C. K. Hall, and W. B. Russel, *J. Colloid Interf. Sci.* **96**, 251 (1983).
- ⁴⁰J. M. Brader and R. Evans, *Physica A* **306**, 287 (2002).
- ⁴¹N. F. Carnahan and K. E. Starling, *J. Chem. Phys.* **51**, 635 (1969).
- ⁴²W. R. Smith and D. Henderson, *Mol. Phys.* **19**, 411 (1970).
- ⁴³M. López de Haro, C. F. Tejero, and A. Santos, *J. Chem. Phys.* **138**, 161104 (2013).
- ⁴⁴L. Rovigatti, N. Gnan, A. Parola, and E. Zaccarelli, *Soft Matter* **11**, 692 (2015).
- ⁴⁵J. L. Lebowitz and J. S. Rowlinson, *J. Chem. Phys.* **41**, 133 (1964).
- ⁴⁶T. Biben and J.-P. Hansen, *Phys. Rev. Lett.* **66**, 2215 (1991).
- ⁴⁷A. Malijevský, S. B. Yuste, and A. Santos, *J. Chem. Phys.* **125**, 074507 (2006).
- ⁴⁸J. Largo, M. A. Miller, and F. Sciortino, *J. Chem. Phys.* **128**, 134513 (2008).
- ⁴⁹G. Stell, *J. Stat. Phys.* **63**, 1203 (1991).
- ⁵⁰E. Zaccarelli, G. Foffi, P. Tartaglia, F. Sciortino, and K. Dawson, *Prog. Colloid Polym. Sci.* **115**, 371 (2000).
- ⁵¹A. Jamnik, *J. Chem. Phys.* **128**, 234504 (2008).
- ⁵²M. Miller and D. Frenkel, *Phys. Rev. Lett.* **90**, 135702 (2003).
- ⁵³M. López de Haro, S. B. Yuste, and A. Santos, in *Theory and Simulation of Hard-Sphere Fluids and Related Systems*, edited by A. Mulero (Springer-Verlag, Berlin, 2008), vol. 753 of *Lecture Notes in Physics*, pp. 183–245.